ACS SENSORS

pubs.acs.org/acssensors Article

Size-Controlled Engineering Photoelectrochemical Biosensor for Human Papillomavirus-16 Based on CRISPR-Cas12a-Induced Disassembly of Z-Scheme Heterojunctions

Yuxuan Li, Ruijin Zeng, Weijun Wang, Jianhui Xu, Hexiang Gong, Ling Li,* Meijin Li,* and Dianping Tang*

Cite This: *ACS Sens.* 2022, 7, 1593−1601 Read Online

ACCESS | Metrics & More | Article Recommendations | Supporting Information

ABSTRACT: Photoelectrochemical (PEC) biosensors incorporating biomolecular recognition with photon-to-electron conversion capabilities of the photoactive species have been developed for molecular diagnosis, but most involve difficulty in adjusting band gap positions and are unsuitable for PEC biodetection. In this work, an innovative PEC biosensor combined with quantum size-controlled engineering based on quantum confinement by controlling the quantum size was designed for the detection of human papillomavirus-16 (HPV-16) through CRISPR-Cas12a (Cpf1)-induced disassembly of Z-scheme heterojunction. To the best of our knowledge, quantum size-controlled engineering that precisely tunes the properties of photoactive materials is first utilized in the PEC bioanalysis. Based on the quantum size effect, the light absorption efficiency and charge-transfer rate were tuned to suitable levels to obtain the best PEC performance. After incubation with target HPV-16, the binding of Cas12a-crRNA to the target double-stranded DNA (dsDNA) stimulated the activity of indiscriminate cleavage toward single-stranded DNA (ssDNA), resulting in a decrease in photocurrent due to the blocking of electron transfer through the heterojunction. By optimizing experimental conditions, the Z-scheme sensing system exhibited incredible photocurrent response to HPV-16 in the range from 3.0 pM to 600 nM with a detection limit of 1.0 pM. Impressively, the application of the quantum size effect could stimulate more interest in the precise design of band gap structure to improve PEC performance.

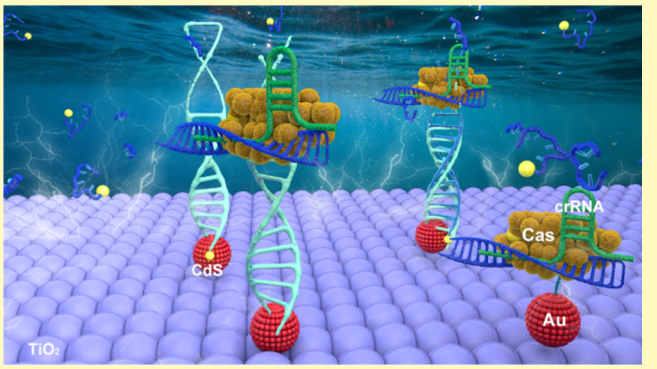

KEYWORDS: *quantum size effect, photoelectrochemical biosensor, Z-scheme, CRISPR-Cas12a, human papillomavirus*

Photoelectrochemical (PEC) biosensor, the main force in the area of multidisciplinary detective methods, has become the focus of the analytical chemistry community.[1] The use of an optical excitation source and an electronic detection signal endows PEC bioanalysis with unique characteristics, such as fast response and a high signal-to-background ratio.[2,3] Photoactive materials, working as a converter to transfer the light source into the electrical signal, play a key role in signal transduction and readout for PEC bioanalysis. Despite the emergence of a variety of photosensitive materials for PEC sensing, it is still difficult to strike the proper balance between band gap and conduction band (CB)/valence band (VB) positions. Moreover, these two factors have a non-negligible impact on the thermodynamic tractive force for reactions, thereby significantly affecting PEC performance.[4] First, the band gap size largely determines the light absorption capacity of materials. Narrow band gap semiconductors allow more efficient utilization of visible light but fail to absorb enough energy to drive the reaction.[5] Second, electron transfer in reactions is deeply influenced by the CB/VB position. For example, Gong's group reported that band energy was related to selectivity and activity of the reaction.[6] Higher energy levels of the CB resulted in a greater driving force for the reaction. Further research by Kamat's team found that when the energy difference between the E_{CB} of the two materials became larger, the driving force for charge transfer increased.[7] In this regard, our motivation is to construct a facile method to balance the band gap and CB/VB positions to construct excellent PEC biosensors.

Many efforts have been devoted to tuning suitable band gap structures, such as doping[8] and heterojunction.[9] Through the formation of a heterojunction, wide band gap semiconductors

Received: April 2, 2022
Accepted: April 27, 2022
Published: May 5, 2022

https://doi.org/10.1021/acssensors.2c00691
ACS Sens. 2022, 7, 1593−1601

Scheme 1. Schematic Illustration of CRISPR-Cas12a-based PEC Biodetection toward HPV-16 by Disassembly of Z-Scheme Heterojunction among TiO_2, Au NPs, and CdS QDs (Au NPs: Gold Nanoparticles, TiO_2: Titanium Dioxide, Cas: CRISPR-Associated Nuclease, crRNA: CRISPR RNA, CdS QDs: Cadmium Sulfide Quantum Dots, HPV-16: Human Papillomavirus-16)

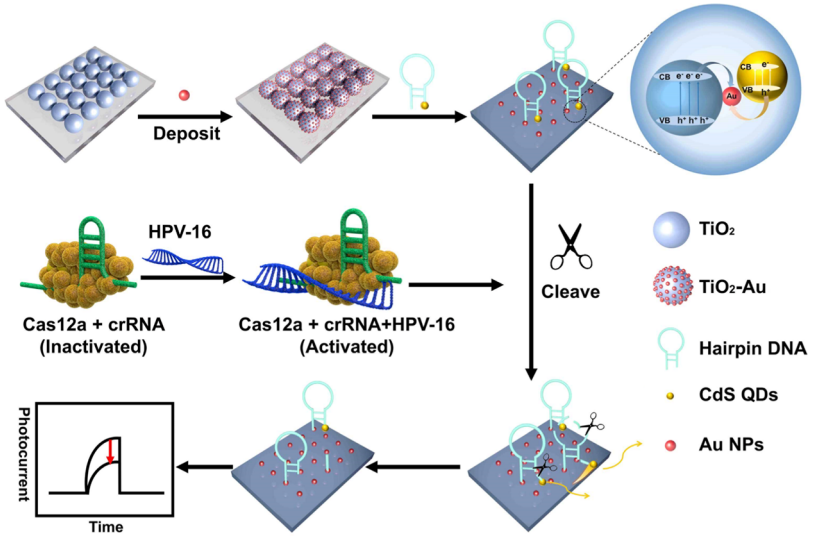

and narrow band gap semiconductors are combined, thus compensating for the shortcoming of the single material.[10] Despite heterojunction being among the most prospective approaches for the development of photoactive materials, there still remain some insurmountable problems in the regulation process. Typically, photogenerated electrons/holes tend to migrate toward lower CB/VB levels during the construction of the heterojunction, which will dramatically diminish the redox ability.[11] Additionally, it is difficult to meet the requirement of precisely adjusting the CB/VB energy levels. Compared with heterojunction construction, the charming property of quantum dots (QDs) such as the quantum confinement effect enables precise regulation of the band structure. As the size of QDs decreases, the originally continuous energy bands then become discrete, leading to a wider band gap and the change of the energy band structure.[12−14] For instance, Osterloh's group presented that E_{CB} and E_{VB} became higher and band gap wider with the decrease of the CdSe QD size.[15] Michael's group demonstrated that the construction of opto-electronic devices could be achieved with the aid of the size-depend effect.[16] Generally speaking, the introduction of quantum size-controlled engineering makes it possible to tailor the band gap structure by controlling the size of QDs. Although there are a wide range of applications of QDs in PEC bioanalysis, quantum size-controlled engineering strategy has been rarely reported. Therefore, exploring the impact of quantum size-controlled engineering on PEC platforms is the emphasis of this work.

In addition to the design of photoactive materials, it is also crucial to find an efficient signal conversion strategy for higher sensitivity of bioanalysis. To date, several strategies have come up, such as enzyme-linked immunosorbent assay,[17] liposome-mediated assay,[18] and DNA technology-assisted strategy.[19] Recently, a DNA technology-assisted strategy, which changes the output signal by destroying the intrinsic heterojunction, has attracted much attention. For example, our group creatively presented a biosensing platform that adjusted the distance between two photoactive materials to decompose the Z-scheme heterojunction.[20] The increasing distance between cadmium sulfide (CdS) QDs and gold nanoparticles (Au NPs) hindered the Z-scheme electron transfer, resulting in the weakening of the photocurrent. Chen's group reported a DNAzyme-induced strategy to disassemble the Z-scheme heterojunction for the change of photocurrent response.[21] The presence of the target lead ion (Pb^{2+}) activated the DNAzyme to cleave connected DNA, inducing a complete separation of CdS QDs from the substrate material. However, the strategies mentioned above still suffer from the problem of being time-consuming and inefficient. Inspiringly, clustered, regularly interspaced, short palindromic repeats (CRISPR)-associated nuclease (Cas)12a proteins and RNA-guided enzymes[22] open a new horizon for amplification strategy due to their unique merits, such as isothermal amplification and strong trans-cleavage activity. For example, Lu's group found that the ambient temperature cleavage of CRISPR-Cas12a allowed for point-of-care diagnostics.[23] Therefore, they constructed a CRISPR-Cas12a-based sensor using aptamers and DNAzymes to modulate the cleavage activity. Moreover, once Cas12a forms a ternary complex with crRNA and the target DNA, the complex shows strong "promiscuous cleavage" activity and cleaves any single-stranded DNA (ssDNA) in the system (called trans-cleavage).[24,25] This undifferentiated cleavage activity can be easily used to cleave hairpin DNA connecting two semiconductors with thousands of flips per second.[26] These properties of CRISPR-Cas12a make it useful in biological recognition and signal transduction.

Human papillomavirus (HPV) is a spherical DNA virus that can be divided into low-risk and high-risk subtypes.[27] A high-risk HPV infection, such as HPV-16, may lead to cell change in the human body, such as in the cervix and anus.[28] Moreover, long-term infections with high-risk HPV can further result in cancer, such as cervical cancer and oropharyngeal cancer.[29] Therefore, it is of great need to develop sensitive and accurate detection methods for high-risk HPVs. Herein, a PEC biosensor based on the titanium dioxide (TiO_2)−Au−CdS QDs Z-scheme system coupled with CRISPR-Cas12a is exploited for the detection of HPV-16 (Scheme 1). With the increase of the QD size from 2.89 to 5.36 nm, the efficiency of

https://doi.org/10.1021/acssensors.2c00691
ACS Sens. 2022, 7, 1593−1601

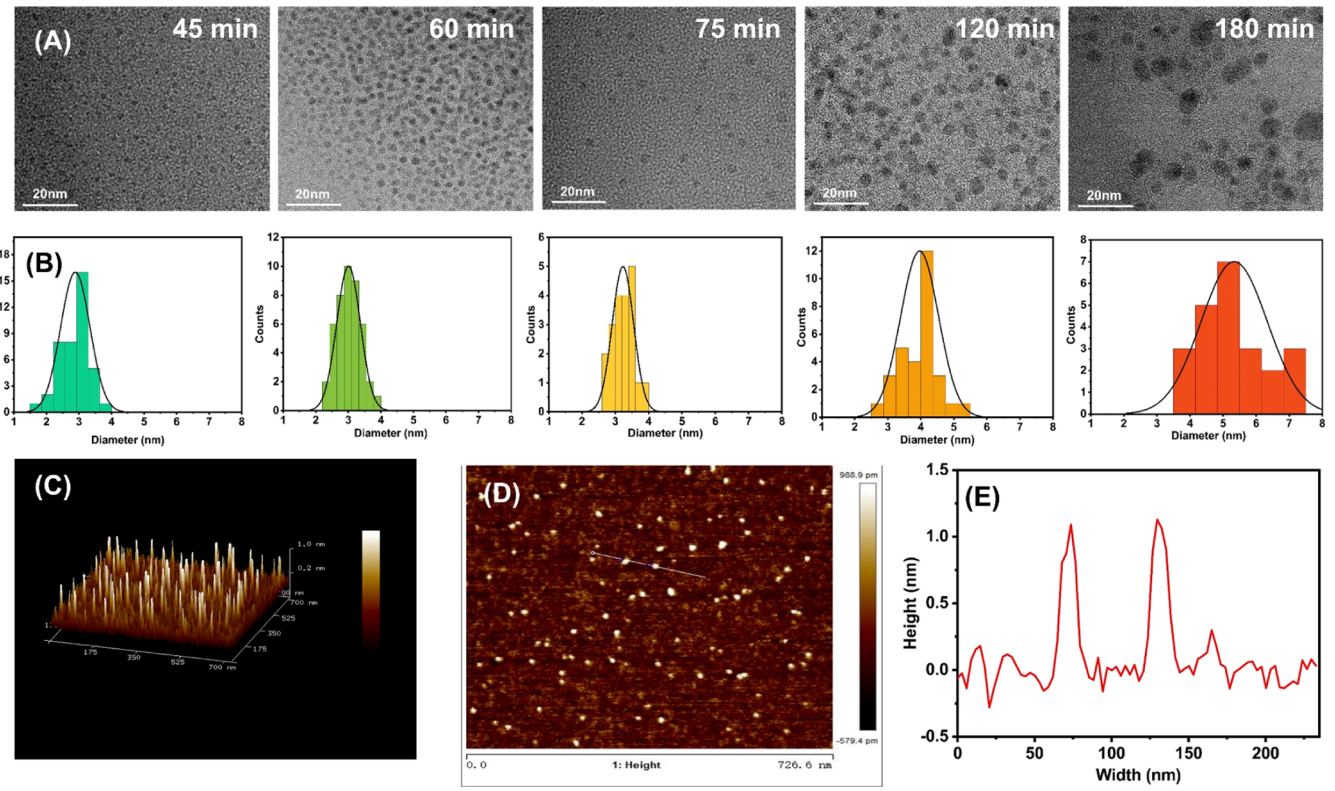

Figure 1. (A) HRTEM images and (B) corresponding size distribution histograms of CdS QDs with different particle sizes (from right to left: 2.89 ± 0.19, 3.01 ± 0.15, 3.23 ± 0.21, 3.96 ± 0.29, and 5.36 ± 0.59 nm); (C) tilted-view and (D) top-view AFM images of CdS QDs (with size of 3.01 ± 0.15 nm); (E) AFM line scan of CdS QDs (marked with white line).

light absorption becomes higher and the electron transfer rate slows down. As the size of QDs is 3.01 nm, these two properties reach an equilibrium point, leading to the best PEC performance. The Z-scheme heterojunction consists primarily of CdS QDs, Au NPs, and TiO_2 nanospheres. Upon the detection of target HPV-16, the Cas12a protein is activated to (trans-) cleave hairpin DNA, which triggers the disassembly of the Z-scheme heterojunction and results in the decrease of the photocurrent.

RESULTS AND DISCUSSION

Characteristics of CdS QDs, TiO_2, TiO_2−Au, and TiO_2−Au−CdS QDs. Homogeneous morphological CdS QDs of different sizes were synthesized by the hydrothermal method with different reaction times. As seen in the transmission electron microscopy (TEM; FEI Talo F200S) image of Figure 1A,B, the sizes of CdS QDs were identified to be 2.89 ± 0.19, 3.01 ± 0.15, 3.23 ± 0.21, 3.96 ± 0.29, and 5.36 ± 0.59 nm, which gradually increased with the increase of heating time (from small to large: 45, 60, 75, 120, and 180 min). The high-resolution TEM (HRTEM) image (Figure S1) revealed a quasi-spherical structure and good crystallinity of pure CdS QDs. Moreover, the atomic force microscopy (AFM) images (Figure 1C,D) of CdS QDs with an optimum size (3.01 ± 0.15 nm) depicted the uniform distribution of QDs, and the AFM line scan (Figure 1E) illustrated its ultrathin thickness, which was about 1.0 nm.

To investigate the PEC performance after sensitization by size-dependent effect of CdS QDs, different TiO_2−Au−CdS QDs were synthesized using the TiO_2−Au nanocomposite as a substrate material. The nanostructure and morphology of the fabricated TiO_2−Au nanomaterials were first investigated by TEM and scanning electron microscopy (SEM; Quanta 250). Specifically, the TiO_2−Au nanocomposites were acquired by three major steps. First, precursor TiO_2 beads with a smooth surface and an average size of about 690 nm were self-assembled through the sol−gel process (Figure S2). After solvothermal treatment, anatase TiO_2 nanospheres shrank in size (diameter of about 520 nm) and have a rougher surface compared with precursor TiO_2 (Figure 2A,D).[30] Afterward, the gold particles were uniformly deposited on the surface of TiO_2 beads by the sodium citrate reduction method. The as-prepared TiO_2−Au nanocomposites retained the intrinsic morphology and dimension because the particle size of Au NPs was too small relative to TiO_2 (Figure 2B,E). More details about TiO_2 and TiO_2−Au regarding their molecular vibration information and crystal structure were further investigated. One strong peak at 144 cm^{-1} and three weak peaks at 395, 515, and 639 cm^{-1} were attributed to the Raman activity modes (E_g, B_{1g}, A_{1g}, and E_g) of anatase TiO_2, suggesting the successful synthesis of anatase TiO_2 (Figure S3).[31,32] However, there was no additional change in the Raman spectra of TiO_2−Au nanocomposites, which could be attributed to the relatively small amount of Au.[33] To prove the existence of gold nanoparticles, X-ray diffraction (XRD; RIGAKU Ultima IV, Japan) was utilized to study the crystalline phase of nanocomposites. The XRD spectrum of TiO_2 showed eight prominent diffraction peaks at 25.28, 37.80, 48.05, 53.89, 62.12, 68.76, 70.31, and 75.03°, which were allocated to the (101), (004), (200), (105), (213), (116), (220), and (215) planes of standard anatase TiO_2 (JCPDS 21-1272) (Figure 2C), confirming the high crystallinity of TiO_2. Notably, new diffraction peaks appeared at 38.18, 44.39, 64.58, and 77.55°,

https://doi.org/10.1021/acssensors.2c00691
ACS Sens. 2022, 7, 1593−1601

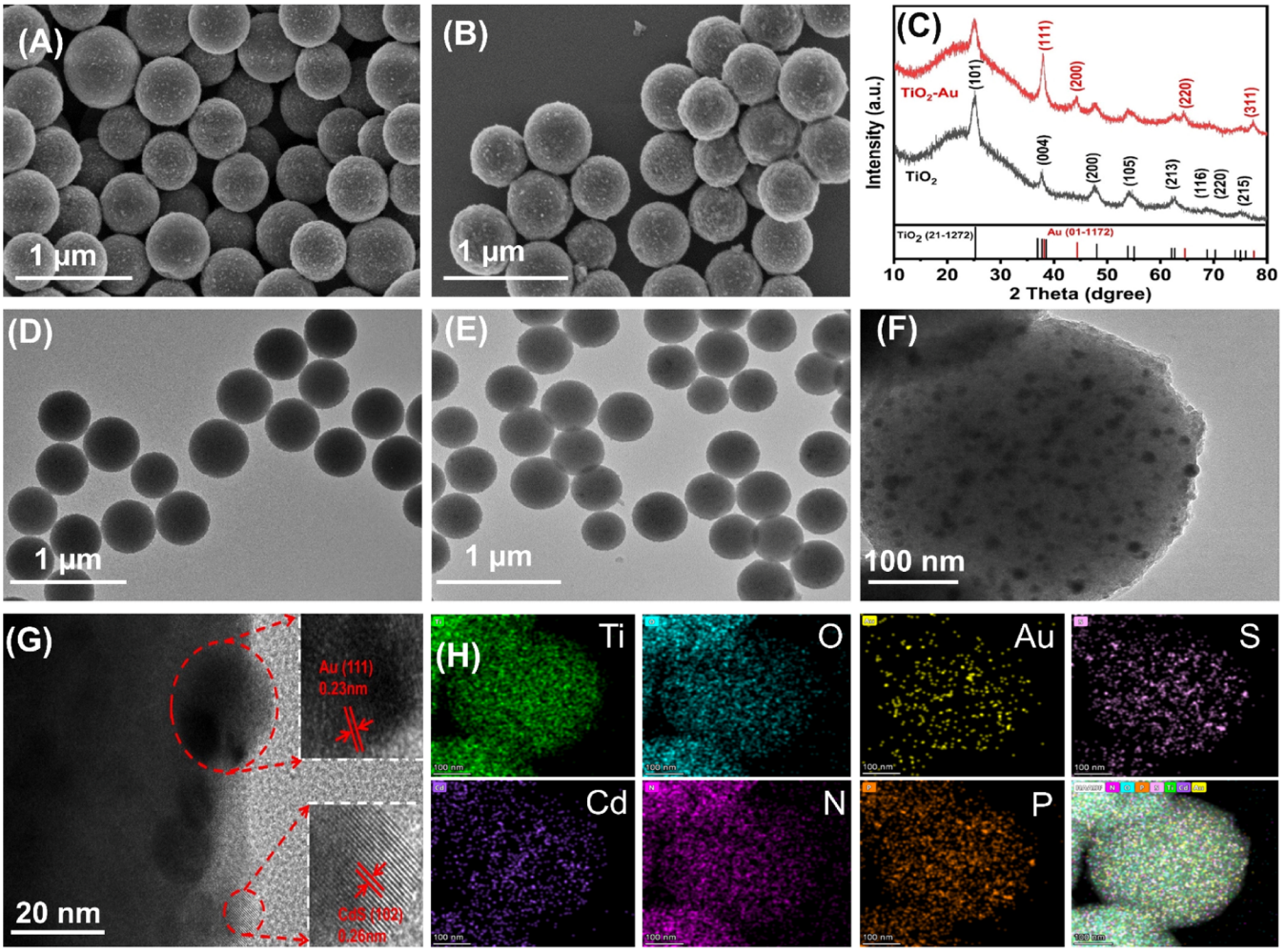

Figure 2. (A,D) SEM and TEM images of TiO_2 nanospheres; (B,E) SEM and TEM images of TiO_2−Au nanocomposites; (C) XRD patterns of TiO_2 and TiO_2−Au nanocomposites; (F,G) HRTEM images of TiO_2−Au−CdS nanocomposites; (H) HAADF-STEM image and elemental mapping for Ti, O, Au, S, Cd, N, and P of TiO_2−Au−CdS nanocomposite.

which were assigned to the (111), (200), (220), and (311) planes of Au (JCPDS 01-1172), revealing the deposition of Au NPs on TiO_2 nanospheres.

After the coupling of CdS QDs to the surface of TiO_2−Au via amino/thiol-modified ssDNA, TiO_2−Au−CdS QDs were obtained through Au−S bond and EDC/NHS activation. HRTEM image (Figure 2F) of TiO_2−Au−CdS QDs demonstrated uniform dispersion of Au NPs on TiO_2 nanospheres, further supporting the successful deposition of Au NPs. The spacing of the lattice intervals of Au NPs and CdS QDs was 0.23 nm and 0.26 nm (Figure 2G) corresponding to the crystal plane (111) of Au and (102) of CdS, respectively.[34] However, it was difficult to observe CdS QDs due to the small size and the high background substrate. Therefore, the elemental mapping analysis (Figure 2H) and the EDS spectrum (Figure S4) of the TiO_2−Au−CdS QDs were utilized to explore the existence of CdS QDs. The coexistence dispersion of Ti, O, Au, Cd, S, N, and P elements throughout the nanostructure indicated that ssDNA was able to attach CdS QDs to the TiO_2−Au surface.

To fully demonstrate the connection and the chemical valence, the change of the TiO_2−Au−CdS nanocomposite before [curve TiO_2−Au−CdS (+)] and after [curve TiO_2−Au−CdS (−)] cleavage activity by Cas12a was investigated by X-ray photoelectron spectroscopy (XPS; Thermo Scientific K-Alpha). As seen in Figure 3A, all elements (Ti 2p; O 1s; Au 4f; Cd 3d; S 2p) associated with TiO_2−Au−CdS composites coexisted. Two characteristic peaks, located at 458.8 and 464.7 eV, were attributed to Ti^{4+} $2p_{3/2}$ and Ti^{4+} $2p_{1/2}$ (Figure 3B). The major peaks of O 1s appeared at 530.3 eV, ascribed to the Ti−O bond in TiO_2 nanospheres (Figures 3C and S5). Meanwhile, the Au 4f spectrum showed two peaks at 83.4 and 87.1 eV, affirming the presence of the Au^0 state (Figure 3D). The Cd 3d could be split into double peaks at 405.5 and 412.3 eV, which were consistent with the positions of Cd $2d_{5/2}$ and Cd $2d_{3/2}$ (Figure 3E).[35] Based on the results obtained from the above characterization, we could conclude that TiO_2−Au−CdS nanocomposites have been successfully synthesized. Besides, the peak intensity of S 2p, Cd 3d, and N 1s (Figures 3E,F and S6) was significantly attenuated after the cleavage, whereas the peak intensity of Ti 2p, O 1s, and Au 4f (Figure 3B−D) diminished. According to the formula $X_A = \frac{I_A / I_A^{\infty}}{\sum I_B / I_B^{\infty}}$, the molar fractions of elements were proportional to their intensity in the XPS spectrum.[36] The molar ratio of Cd, S, and N elements significantly decreased, while the molar ratio of Ti, O, and Au elements increased relatively because of the breaking of QD-HP (CdS QDs-connected hairpin DNA). Therefore, the enhancement and weakening of the above XPS

https://doi.org/10.1021/acssensors.2c00691
ACS Sens. 2022, 7, 1593−1601

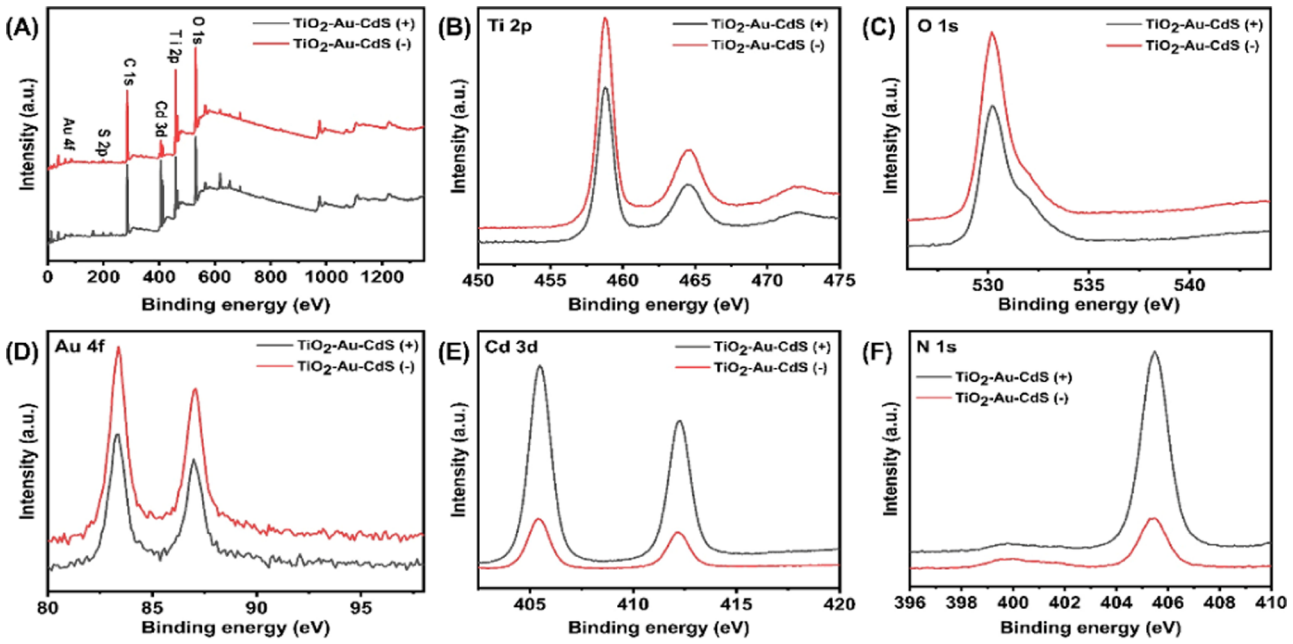

Figure 3. XPS survey spectra of (A) TiO_2−Au−CdS; (B) Ti 2p; (C) O 1s; (D) Au 4f; (E) Cd 3d; (F) N 1s [curves TiO_2−Au−CdS (+) and TiO_2−Au−CdS (−) represent the TiO_2−Au−CdS before and after the cleavage of activated Cas12a].

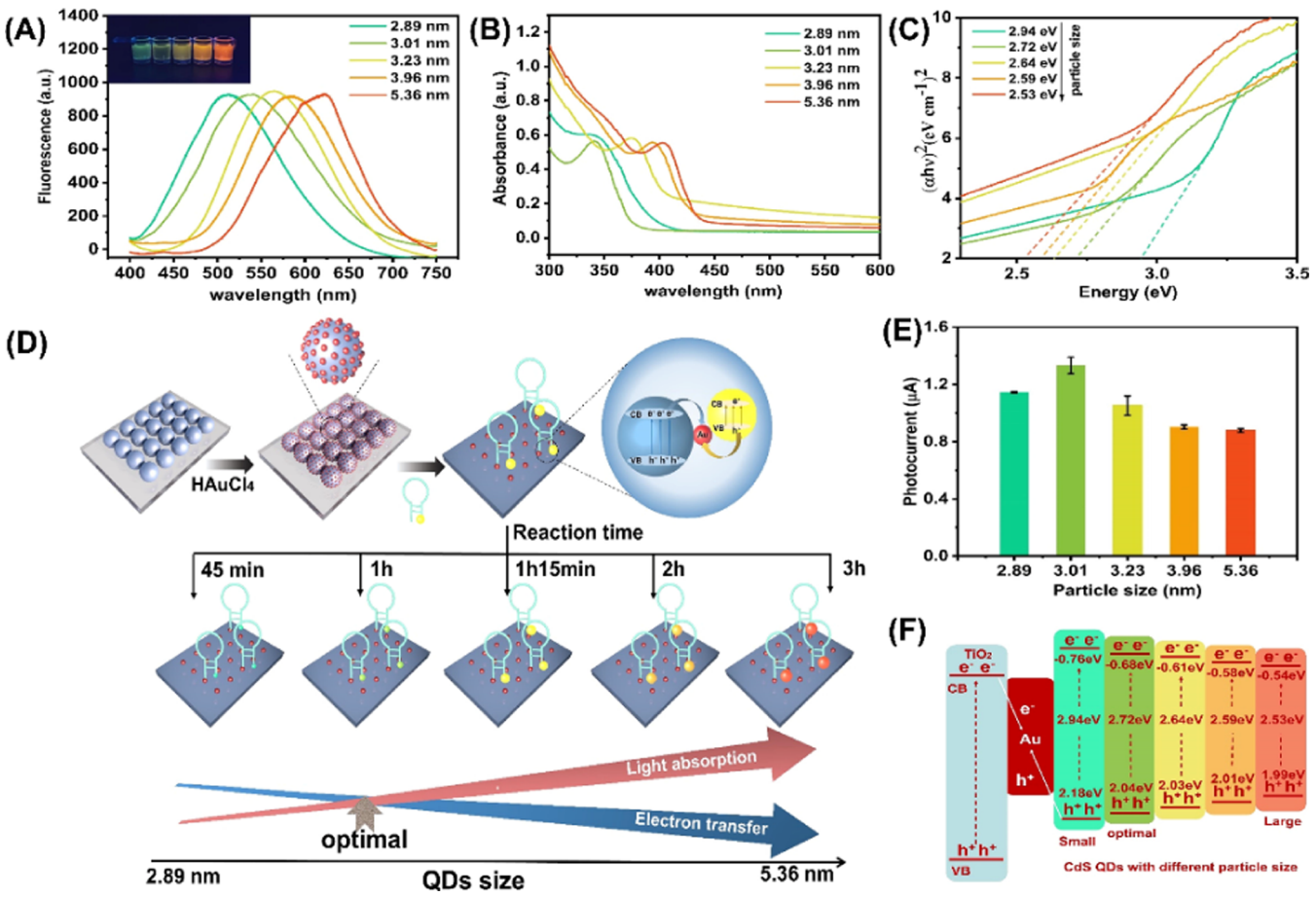

Figure 4. (A) PL spectra (inset: digital photograph under UV light); (B) UV−vis absorption spectra; (C) tauc plot from UV−vis analysis; (E) photocurrent of TiO_2−Au sensitized with different sizes of CdS QDs; (D) schematic illustration of the size effect; (F) energy band diagram of the TiO_2−Au−CdS heterojunction.

spectral intensity, on the one hand, could indicate that CdS QDs were successfully attached to the TiO_2−Au nanocomposite by carbodiimide coupling and, on the other hand, also confirmed the DNAzyme activity of Cas12a.

https://doi.org/10.1021/acssensors.2c00691
ACS Sens. 2022, 7, 1593−1601

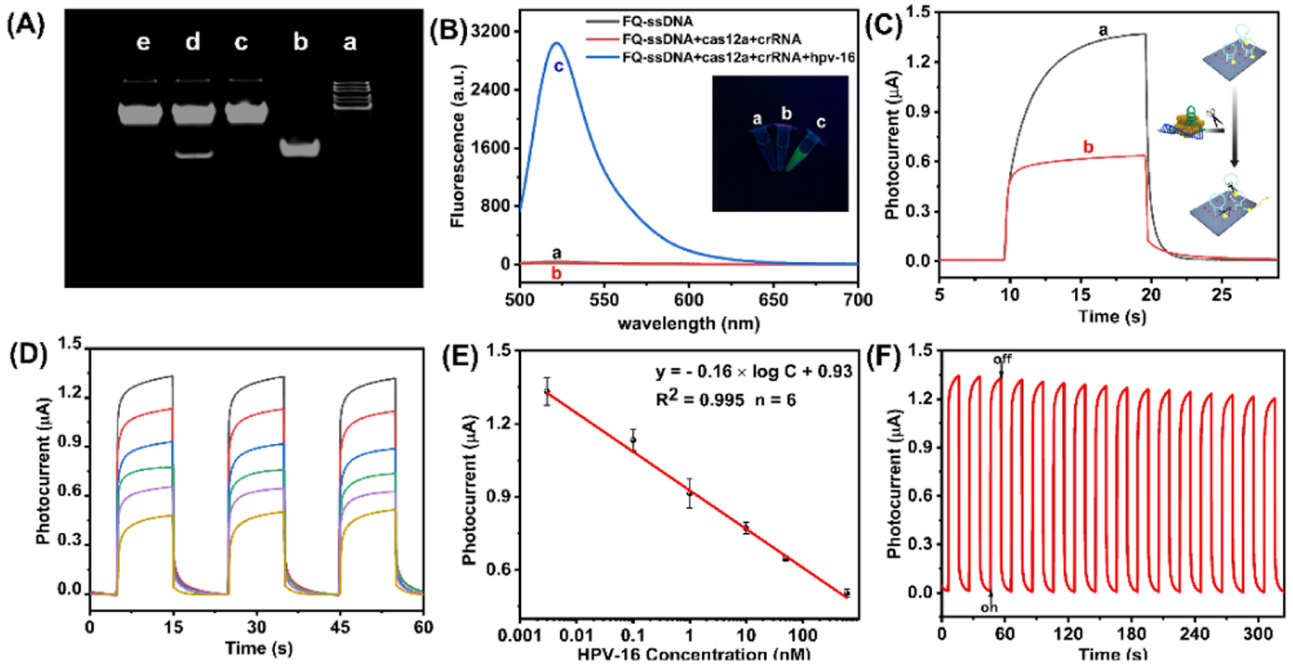

Figure 5. (A) PAGE image (12% gel) for different samples (lane "a": DNA-marker; lane "b": 500 nM ssDNA; lane "c": 500 nM HPV-16 + 500 nM ssDNA; lane "d": 500 nM HPV-16 + 500 nM ssDNA + crRNA + Cas 12a); (B) fluorescence analysis (a.u.) of (a) FQ-ssDNA, (b) FQ-ssDNA + crRNA + Cas12a, and (c) FQ-ssDNA + crRNA + Cas12a + HPV-16 (inset: corresponding fluorescence image); (C) photocurrent responses of (a) TiO_2−Au−CdS QDs/FTO and (b) TiO_2−Au−CdS QDs/FTO after incubation with 50 nM HPV-16 + crRNA + Cas12a; (D) photocurrent concentration gradient image of Crispr-Cas12a-based TiO_2−Au−CdS QDs biosensing platform toward target HPV-16 with different concentrations including 0.003, 0.01, 0.1, 10, 50, and 600 nM [substrate: 10 mM PBS (pH 7.4) including 1.0 mM ascorbic acid and 0.1 M Na_2SO_4]; (E) linear correlation; (F) stability of the TiO_2−Au−CdS QDs/FTO bioanalysis system.

Size Effect of CdS QDs. In order to explore the size effect on PEC performance, an analysis toward the sizeable influence on the optical properties of QDs was performed. Photograph of QDs under ultraviolet (UV) excitation (Figure 4A) was the most obvious sign of quantum confinement, which corresponded to the photoluminescence (PL) peak positions of 511.4, 539.1, 564.8, 582.2, and 622.6 nm. As shown in Figure 4B, the absorption peaks of UV−vis (visible) spectra were located at 336, 341, 374, 393, and 402 nm, ascribed to 1sh-1se excitonic transitions.[37] The absorption peak red-shifted with the increase of particle size, which indicated that visible light absorption tended to intensify with the expansion of size. In accordance with the result above, the band gap of CdS QDs (Figure 4C; calculated by the formula $(\alpha h\nu)^2 = A(h\nu - E_g$, see details in the Supporting Information) shrunk in a similar way from 2.94 to 2.53 eV. Additionally, to disclose the influence on the band position, the energy level of the CB bottom (E_{CB}) was estimated based on Mott−Schottky plots (Figure S7). Mott−Schottky plots were developed for the flat band potential, which was approximately equivalent to E_{CB}.[38−40] Therefore, the derived potentials of CB maximum of CdS QDs could be approximated as −0.76, −0.68, −0.61, −0.58, and −0.54 eV versus the normal hydrogen electrode. Based on the formula $E_{VB} = E_{CB} + E_g$, the potentials of VB maximum could be calculated as 2.18, 2.04, 2.03, 2.01, and 1.99 eV. It was worth noting that the extrapolated potential (Figures 4F and S8) became higher as the particle size was increased, which facilitated an efficient charge transfer due to the increased driving force, hence boosting better PEC performance.[7,41] As shown in Figure 4D, as the particle size decreases, the light absorption capacity of CdS QDs increases, while the charge transfer rate decreases. Thus, there is a tradeoff between these two properties.

To find the optimized QDs for better PEC bioanalysis, the photocurrent of as-prepared materials sensitized with different particle sizes of QDs was detected. Prior to the modification of CdS QDs, the photocurrents of TiO_2 and TiO_2−Au were measured (Figure S9). The photocurrent of the TiO_2-modified FTO electrode was the weakest (curve "a") on account of the wide band gap of TiO_2 (3.2 eV). After Au NPs were deposited on the surface of TiO_2 nanospheres, the photocurrent increased 2-fold due to the localized surface plasmon resonance effect of Au NPs (curve "b"). After modification with different sizes of QDs, the photocurrent was all exponentially enhanced, indicating the effect of QD sensitization (curve "c"). Furthermore, as the particle size increases, the photocurrent showed a volcano shape trend and reached a maximum at a particle size of 3.01 nm (Figure 4E), which was consistent with the above speculation. Therefore, this result implied that CdS QDs with a diameter of 3.01 nm exhibited the best PEC performance.

Feasibility Investigation. As mentioned above, the change in photocurrent occurred because the Cas12a protein was driven by the target to cleave the CdS QDs, thereby destroying the heterojunction. The cleavage of Cas12a has been initially characterized by XPS above, and we corroborated it by polyacrylamide gel electrophoresis (PAGE; Figure 5A). The difference between lane "b," lane "c," and lane "d" indicated that the target HPV-16 is not destructive to ssDNA in the absence of the Cas12a protein and crRNA. Comparing lane "d" and lane "e", it should be noted that the random ssDNA was subjected to a large degree of fragmentation due to the trans-cleavage activity of the activated-CRISPR-Cas12a

https://doi.org/10.1021/acssensors.2c00691
ACS Sens. 2022, 7, 1593−1601

system. The PAGE result demonstrated the performance of the Cas12a-crRNA-target system in indiscriminately cleaving ssDNA. To extend the conclusion, fluorescence analysis was performed by using FQ ssDNA (ssDNA marked with FAM and BHQ on both sides) as the cleaved substrate. As shown in Figure 5B, in the absence of HPV-16, the fluorophore and quencher kept in close contact since the cleavage activity of Cas12a was inactivated, leading to an inappreciable fluorescent signal (curve "b"). Impressively, once HPV-16 appeared and binned to the Cas-crRNA complex, the FQ ssDNA was cleaved and the fluorescent signal was released (curve "c"). These consistent results revealed that the efficient cleavage toward ssDNA could be triggered by activator HPV-16, which proved the feasibility of the CRISPR-Cas12a mediated PEC biosensor.

Another issue is whether the heterojunction will be disrupted and cause a change in the photocurrent after the cleavage. The validity of this scheme was demonstrated by detecting the photocurrent of the TiO_2−Au−CdS electrode before and after the cleavage of Cas12a (Figure 5C). The CdS QDs with optimum size, Au NPs, and TiO_2 nanospheres formed the Z-scheme heterojunction, causing a maximum photocurrent (curve "a"), indicating that the formation of the Z-scheme heterojunction succeeded in accelerating the transport of electrons. Inspiringly, after the TiO_2−Au−CdS electrode was incubated in the target-Cas-crRNA premix solution, the photocurrent decreased significantly (curve "b"), indicating that the effect of cleavage on the electrode can be reflected in the photocurrent. These findings implied that the CRISPR-Cas12a-based TiO_2−Au−CdS QDs Z-scheme biosensor could be harnessed for the test of HPV-16, which is consistent with the above XPS results.

Analytical Performance of CRISPR-Cas12a-Based TiO_2−Au−CdS QD Z-Scheme Sensing System. By integrating CRISPR-Cas12a with a TiO_2−Au−CdS QDs-based Z-scheme sensing system, the photocurrent of different concentrations of HPV-16 was measured under optimal conditions (Figure S10). As the HPV-16 concentration in the sample increased, the measurable photocurrent trended downward and reached a plateau above 600 nM HPV-16 (Figure 5D). The photocurrent declined linearly as the concentration of target HPV-16 increased from 0.003 to 600 nM, and the linear regression equation could be formulated as I (μA) = 0.93−0.16 × log C ($C_{HPV\text{-}16}$, nM) (R^2 = 0.995, n = 6) (Figure 5E). The limit of detection (LOD) was calculated to be 1.0 pM (S/N = 3). To demonstrate the advantages of the CRISPR Cas12a-based TiO_2−Au−CdS QDs Z-scheme sensing platform, the linear range and LOD of this biosensor were contrasted with other HPV-16 testing methods (Table S1). It was clear that our system showed excellent sensitivity, mainly due to the sensitization with optimal CdS QDs, resulting in the maximum initial photocurrent. In addition, the relative standard deviations (RSDs) were 6.3, 5.9, and 6.2% (n = 3) for intra-assays and 10.8, 10.3, and 11.6% (n = 3) for interassays toward 0.1, 50, and 600 nM HPV-16, suggesting good repeatability. Besides, the stability (RSD = 3.4%) of the constructed biosensing platform was demonstrated by measuring the photocurrent with the xenon lamp on and off for 300 s (Figure 5F). In a word, the modified electrode exhibited excellent stability and reproducibility.

Specificity was also a crucial criterion for the biosensing platform. Therefore, the photocurrent response toward target HPV-16 and other high-risk interfering viruses such as HPV-18 and HPV-13 was measured on the constructed platform. As illustrated in Figure S11, the photocurrent of each interfering virus (600 nM) was essentially the same as the blank value. However, the photocurrent of the mixture (containing 600 nM HPV-16, 600 nM HPV-18, and 600 nM HPV-13), as well as the target HPV-16, showed a significant reduction relative to the blank value, confirming the anti-interference ability of the constructed biosensor.

Screening of Real Human Serum Sample. To investigate the accuracy of the CRISPR-Cas12a-based PEC biosensor, different concentrations of HPV-16 standards including 0.01, 0.1, 1.0, 10, 10, 100, and 500 nM were spiked into human serum specimens. Thereafter, these spiked samples were assayed using the developed PEC biosensor. Finally, the corresponding recoveries were calculated. As shown in Table S2, the recoveries were 99−106%, indicating good accuracy for quantitative monitoring of target HPV-16 in the complex samples.

CONCLUSIONS

In summary, we built an innovative platform to efficiently and sensitively detect HPV-16 by combining quantum size-controlled engineering with an efficient CRISPR-Cas12a cleavage system. The size effect based on quantum confinement was applied in the PEC biosensor. Compared with conventional PEC sensing methods, the advantages of this work can be simply summarized as follows: (i) introduction of quantum size-controlled engineering makes it possible to precisely adjust the band gap structure of materials, thus leading to the perfect PEC performance; (ii) strategy of altering the photocurrent by complete disassembly of the heterojunction allows for more significant signal amplification; and (iii) introduction of CRISPR-Cas12a enables an isothermal signal amplification and a more efficient strategy compared to other signal conversion strategies that disassociate the heterojunctions. Nevertheless, the drawbacks of this biosensor still exist. For example, the connection of TiO_2−Au nanospheres to CdS QDs *via* DNA may be inefficient and time-consuming. Therefore, future work should be devoted to finding a better way to integrate photoactive materials. Importantly, this biosensing platform offers an inspiration for the construction of other PEC sensors to exploit quantum confinement effects on photoactive materials.

EXPERIMENTAL SECTION

Fabrication of TiO_2 Nanospheres. Hexadecylamine (0.88 g) and anhydrous ethanol (100 mL) were added to a 250 mL beaker and stirred until completely dissolved, then dropwise added potassium chloride solution (KCl, 0.1 M, 0.4 mL) for the modulation of the ionic strength, followed by ultrapure water (0.25 mL). Subsequently, titanium(IV) isopropoxide (2.16 mL) was added to the above solution under vigorous stirring at room temperature. After the stewing-centrifugation (stewing time was 18 h) process, the sample was rinsed with ethanol and dried at 75 °C overnight. The mixture of the sample, ultrapure water, and ethanol (the ratio of sample/ultrapure water/ethanol = 0.5 g:10 mL:20 mL) was added into a 100 mL Teflon-lined autoclave and then maintained at 160 °C for 90 min. The obtained TiO_2 nanospheres were obtained by the same post-treatment as above.

Target Determination and PEC Measurement. Target double-stranded DNA (dsDNA) was prepped by coincubating target HPV-16 (10 μL) with nontarget ssDNA (10 μL) in ultrapure water (180 μL) at 95 °C for 5 min and annealing for 20 min. Meanwhile, Cas12a protein (100 nM, 5 μL, 2 μL of 10 × NEBuffer 2.1) and crRNA (260 nM, 2 μL, in RNase free buffer) were incubated at room temperature for 30 min. Subsequently, target dsDNA (20 μL) with different

https://doi.org/10.1021/acssensors.2c00691
ACS Sens. 2022, 7, 1593−1601

concentrations were added into Cas12a-crRNA (20 μL) for 30 min of incubation at RT. Then, the mixture was dripped onto TiO_2−Au−CdS-modified FTO and incubated for 50 min. In the process, the single-stranded portion of hairpin DNA connected with CdS QDs and Au NPs was cut by Cas12a, causing the CdS QDs to leave the electrode surface. The photocurrent was measured by an electrochemical workstation (CHI660, China), where the modified FTO served as the working electrode.

■ ASSOCIATED CONTENT

Supporting Information

The Supporting Information is available free of charge at https://pubs.acs.org/doi/10.1021/acssensors.2c00691.

Materials and reagents; fabrication of TiO_2−Au nanocomposites, synthesis of MPA-capped CdS QDs, fabrication of CdS QD-labeled hairpin DNA, fabrication of PEC biosensing platform, and additional figures and tables (PDF)

■ AUTHOR INFORMATION

Corresponding Authors

Ling Li − *The First Clinical Medical College of Fujian Medical University, Fuzhou 350004, People's Republic of China; Hepatopancreatobiliary Surgery Department, The First Affiliated Hospital of Fujian Medical University, Fuzhou 350004, People's Republic of China*; Phone: +86-591-2286 6125; Email: drliling@126.com; Fax: +86-591-2286 6135

Meijin Li − *Key Laboratory for Analytical Science of Food Safety and Biology (MOE & Fujian Province), Department of Chemistry, Fuzhou University, Fuzhou 350108, People's Republic of China*; orcid.org/0000-0002-8245-5556; Email: mjli@fzu.edu.cn

Dianping Tang − *Key Laboratory for Analytical Science of Food Safety and Biology (MOE & Fujian Province), Department of Chemistry, Fuzhou University, Fuzhou 350108, People's Republic of China*; orcid.org/0000-0002-0134-3983; Email: dianping.tang@fzu.edu.cn

Authors

Yuxuan Li − *Key Laboratory for Analytical Science of Food Safety and Biology (MOE & Fujian Province), Department of Chemistry, Fuzhou University, Fuzhou 350108, People's Republic of China*

Ruijin Zeng − *Key Laboratory for Analytical Science of Food Safety and Biology (MOE & Fujian Province), Department of Chemistry, Fuzhou University, Fuzhou 350108, People's Republic of China*

Weijun Wang − *Key Laboratory for Analytical Science of Food Safety and Biology (MOE & Fujian Province), Department of Chemistry, Fuzhou University, Fuzhou 350108, People's Republic of China*

Jianhui Xu − *Key Laboratory for Analytical Science of Food Safety and Biology (MOE & Fujian Province), Department of Chemistry, Fuzhou University, Fuzhou 350108, People's Republic of China*

Hexiang Gong − *Key Laboratory for Analytical Science of Food Safety and Biology (MOE & Fujian Province), Department of Chemistry, Fuzhou University, Fuzhou 350108, People's Republic of China*

Complete contact information is available at: https://pubs.acs.org/10.1021/acssensors.2c00691

Notes

The authors declare no competing financial interest.

■ ACKNOWLEDGMENTS

The authors acknowledge the financial support from the National Natural Science Foundation of China (grant nos.: 21874022 and 21675029).

■ REFERENCES

(1) Shu, J.; Tang, D. Current advances in quantum-dots-based photoelectrochemical immunoassays. *Chem.—Asian J.* **2017**, *12*, 2780−2789.

(2) Zhao, W.-W.; Xu, J.-J.; Chen, H.-Y. Photoelectrochemical enzymatic biosensors. *Biosens. Bioelectron.* **2017**, *92*, 294−304.

(3) Li, Y.; Wang, W.; Gong, H.; Xu, J.; Yu, Z.; Wei, Q.; Tang, D. Graphene-coated copper-doped ZnO quantum dots for sensitive photoelectrochemical bioanalysis of thrombin triggered by DNA nanoflowers. *J. Mater. Chem. B* **2021**, *9*, 6818−6824.

(4) Chen, S.; Huang, D.; Xu, P.; Xue, W.; Lei, L.; Cheng, M.; Wang, R.; Liu, X.; Deng, R. Semiconductor-based photocatalysts for photocatalytic and photoelectrochemical water splitting: will we stop with photocorrosion? *J. Mater. Chem. A* **2020**, *8*, 2286−2322.

(5) Joy, J.; Mathew, J.; George, S. C. Nanomaterials for photoelectrochemical water splitting − review. *Int. J. Hydrogen Energy* **2018**, *43*, 4804−4817.

(6) Li, A.; Wang, T.; Li, C.; Huang, Z.; Luo, Z.; Gong, J. Adjusting the reduction potential of electrons by quantum confinement for selective photoreduction of CO_2 to methanol. *Angew. Chem., Int. Ed.* **2019**, *58*, 3804−3808.

(7) Chakrapani, V.; Tvrdy, K.; Kamat, P. V. Modulation of electron injection in CdSe−TiO_2 system through medium alkalinity. *J. Am. Chem. Soc.* **2010**, *132*, 1228−1229.

(8) Zhang, K.; Lv, S.; Lin, Z.; Tang, D. CdS:Mn quantum dot-functionalized g-C_3N_4 nanohybrids as signal-generation tags for photoelectrochemical immunoassay of prostate specific antigen coupling DNAzyme concatamer with enzymatic biocatalytic precipitation. *Biosens. Bioelectron.* **2017**, *95*, 34−40.

(9) Zeng, R.; Zhang, L.; Su, L.; Luo, Z.; Zhou, Q.; Tang, D. Photoelectrochemical bioanalysis of antibiotics on rGO-Bi_2WO_6-Au based on branched hybridization chain reaction. *Biosens. Bioelectron.* **2019**, *133*, 100−106.

(10) Lv, S.; Zhang, K.; Zhu, L.; Tang, D. ZIF-8-Assisted NaYF4:Yb,Tm@ZnO converter with exonuclease III-Powered DNA walker for Near-Infrared light responsive biosensor. *Anal. Chem.* **2020**, *92*, 1470−1476.

(11) Low, J.; Yu, J.; Jaroniec, M.; Wageh, S.; Al-Ghamdi, A. Heterojunction photocatalysts. *Adv. Mater.* **2017**, *29*, 1601649.

(12) Bera, D.; Qian, L.; Tseng, T.-K.; Holloway, P. H. Quantum dots and their multimodal applications: A review. *Materials* **2010**, *3*, 2260−2345.

(13) Smith, A. M.; Nie, S. Semiconductor nanocrystals: structure, properties, and band gap engineering. *Acc. Chem. Res.* **2010**, *43*, 190−200.

(14) Wise, F. W. Lead salt quantum dots: the limit of strong quantum confinement. *Acc. Chem. Res.* **2000**, *33*, 773−780.

(15) Zhao, J.; Holmes, M. A.; Osterloh, F. E. Quantum confinement controls photocatalysis: A free energy analysis for photocatalytic proton reduction at CdSe nanocrystals. *ACS Nano* **2013**, *7*, 4316−4325.

(16) Ummadisingu, A.; Meloni, S.; Mattoni, A.; Tress, W.; Grätzel, M. Crystal-Size-Induced band gap tuning in perovskite films. *Angew. Chem., Int. Ed.* **2021**, *60*, 21368−21376.

(17) Yu, Z.; Huang, L.; Chen, J.; Tang, Y.; Xia, B.; Tang, D. Full-spectrum responsive photoelectrochemical immunoassay based on β-In2S3@carbon dot nanoflowers. *Electrochim. Acta* **2020**, *332*, 135473.

(18) Xu, J.; Li, Y.; Gong, H.; Yu, Z.; Zhang, J.; Wei, Q.; Tang, D. Au nanoparticle-decorated ZnO microflower-based immunoassay for

photoelectrochemical detection of human prostate-specific antigen. *ACS Appl. Nano Mater.* **2021**, *4*, 10943−10951.
(19) Gong, H.; Wu, Y.; Zeng, R.; Zeng, Y.; Liu, X.; Tang, D. CRISPR/Cas12a-mediated liposome-amplified strategy for the photoelectrochemical detection of nucleic acid. *Chem. Commun.* **2021**, *57*, 8977−8980.
(20) Zeng, R.; Luo, Z.; Su, L.; Zhang, L.; Tang, D.; Niessner, R.; Knopp, D. Palindromic molecular beacon based Z-scheme BiOCl-Au-CdS photoelectrochemical biodetection. *Anal. Chem.* **2019**, *91*, 2447−2454.
(21) Meng, L.; Liu, M.; Xiao, K.; Zhang, X.; Du, C.; Chen, J. Sensitive photoelectrochemical assay of $Pb^{(2+)}$ based on DNAzyme-induced disassembly of the "Z-scheme" TiO_2/Au/CdS QDs system. *Chem. Commun.* **2020**, *56*, 8261−8264.
(22) Chen, J. S.; Ma, E.; Harrington, L. B.; Da Costa, M.; Tian, X.; Palefsky, J. M.; Doudna, J. A. CRISPR-Cas12a target binding unleashes indiscriminate single-stranded DNase activity. *Science* **2018**, *360*, 436−439.
(23) Xiong, Y.; Zhang, J.; Yang, Z.; Mou, Q.; Ma, Y.; Xiong, Y.; Lu, Y. Functional DNA regulated CRISPR-Cas12a sensors for point-of-care diagnostics of non-nucleic-acid targets. *J. Am. Chem. Soc.* **2020**, *142*, 207−213.
(24) Li, S.-Y.; Cheng, Q.-X.; Liu, J.-K.; Nie, X.-Q.; Zhao, G.-P.; Wang, J. CRISPR-Cas12a has both cis- and trans-cleavage activities on single-stranded DNA. *Cell Res.* **2018**, *28*, 491−493.
(25) Zeng, R.; Wang, W.; Chen, M.; Wan, Q.; Wang, C.; Knopp, D.; Tang, D. CRISPR-Cas12a-driven MXene-PEDOT:PSS piezoresistive wireless biosensor. *Nano Energy* **2021**, *82*, 105711.
(26) Peng, S.; Tan, Z.; Chen, S.; Lei, C.; Nie, Z. Integrating CRISPR-Cas12a with a DNA circuit as a generic sensing platform for amplified detection of microRNA. *Chem. Sci.* **2020**, *11*, 7362−7368.
(27) Jacobs, M. V.; Snijders, P. J.; van den Brule, A. J.; Helmerhorst, T. J.; Meijer, C. J.; Walboomers, J. M. A general primer GP5+/GP6(+)-mediated PCR-enzyme immunoassay method for rapid detection of 14 high-risk and 6 low-risk human papillomavirus genotypes in cervical scrapings. *J. Clin. Microbiol.* **1997**, *35*, 791−795.
(28) Castellsagué, X. Natural history and epidemiology of HPV infection and cervical cancer. *Gynecol. Oncol.* **2008**, *110*, S4−S7.
(29) Crosbie, E. J.; Einstein, M. H.; Franceschi, S.; Kitchener, H. C. Human papillomavirus and cervical cancer. *Lancet* **2013**, *382*, 889−899.
(30) Chen, D.; Cao, L.; Huang, F.; Imperia, P.; Cheng, Y.-B.; Caruso, R. A. Synthesis of monodisperse mesoporous titania beads with controllable diameter, high surface areas, and variable pore diameters (14−23 nm). *J. Am. Chem. Soc.* **2010**, *132*, 4438−4444.
(31) Choi, H. C.; Jung, Y. M.; Kim, S. B. Size effects in the Raman spectra of TiO_2 nanoparticles. *Vib. Spectrosc.* **2005**, *37*, 33−38.
(32) Zhang, J.; Li, M.; Feng, Z.; Chen, J.; Li, C. UV Raman spectroscopic study on TiO_2. I. phase transformation at the surface and in the bulk. *J. Phys. Chem. C* **2006**, *110*, 927−935.
(33) Elsayed, K. A.; Alomari, M.; Drmosh, Q. A.; Manda, A. A.; Haladu, S. A.; Olanrewaju Alade, I. Anticancer activity of TiO_2/Au nanocomposite prepared by laser ablation technique on breast and cervical cancers. *Opt. Laser Technol.* **2022**, *149*, 107828.
(34) Xia, L.; Xu, L.; Song, J.; Xu, R.; Liu, D.; Dong, B.; Song, H. CdS quantum dots modified CuO inverse opal electrodes for ultrasensitive electrochemical and photoelectrochemical biosensor. *Sci. Rep.* **2015**, *5*, 10838.
(35) Zeng, R.; Lian, K.; Su, B.; Lu, L.; Lin, J.; Tang, D.; Lin, S.; Wang, X. Versatile synthesis of hollow metal sulfides via reverse cation exchange reactions for photocatalytic CO_2 reduction. *Angew. Chem., Int. Ed.* **2021**, *60*, 25055−25062.
(36) Seah, M. P. The quantitative analysis of surfaces by XPS: A review. *Surf. Interface Anal.* **1980**, *2*, 222−239.
(37) Matsumoto, H.; Sakata, T.; Mori, H.; Yoneyama, H. preparation of monodisperse CdS nanocrystals by size selective photocorrosion. *J. Phys. Chem.* **1996**, *100*, 13781−13785.
(38) Gelderman, K.; Lee, L.; Donne, S. W. Flat-band potential of a semiconductor: using the Mott Schottky equation. *J. Chem. Educ.* **2007**, *84*, 685−688.
(39) Wang, S.; Guan, B. Y.; Lu, Y.; Lou, X. W. D. Formation of hierarchical In_2S_3−$CdIn_2S_4$ heterostructured nanotubes for efficient and stable visible light CO_2 reduction. *J. Am. Chem. Soc.* **2017**, *139*, 17305−17308.
(40) Tao, R.; Zhao, C.; Shao, C.; Li, X.; Li, X.; Zhang, J.; Yang, S.; Liu, Y. Bi_2WO_6/$ZnFe_2O_4$ heterostructures nanofibers: enhanced visible-light photocatalytic activity and magnetically separable property. *Mater. Res. Bull.* **2018**, *104*, 124−133.
(41) Leventis, H. C.; O'Mahony, F.; Akhtar, J.; Afzaal, M.; O'Brien, P.; Haque, S. A. Transient optical studies of interfacial charge transfer at nanostructured metal oxide/PbS quantum dot/organic hole conductor heterojunctions. *J. Am. Chem. Soc.* **2010**, *132*, 2743−2750.

https://doi.org/10.1021/acssensors.2c00691
ACS Sens. 2022, 7, 1593−1601